JGR Solid Earth

RESEARCH ARTICLE
10.1029/2022JB026148

Crustal Structure of the Western U.S. From Rayleigh and Love Wave Amplification Data

William Sturgeon[1], **Ana M. G. Ferreira**[1,2], **Lewis Schardong**[3], **and Augustin Marignier**[4]

[1]Department of Earth Sciences, Faculty of Mathematical & Physical Sciences, University College London, London, UK, [2]CERIS, Instituto Superior Técnico, Universidade de Lisboa, Lisboa, Portugal, [3]The Geological Survey of Israel, Jerusalem, Israel, [4]Research School of Earth Sciences, Australian National University, Canberra, Australia

Key Points:

- Love wave amplification measurements are used for the first time and are jointly inverted with Rayleigh wave amplification measurements
- We perform extensive synthetic tests to quantify the advantages and limitations of our approach
- We present SWUS-crust, a new crustal model of the western U.S.

Supporting Information:

Supporting Information may be found in the online version of this article.

Correspondence to:

W. Sturgeon,
william.sturgeon.12@ucl.ac.uk

Citation:

Sturgeon, W., Ferreira, A. M. G., Schardong, L., & Marignier, A. (2023). Crustal structure of the western U.S. from Rayleigh and Love wave amplification data. *Journal of Geophysical Research: Solid Earth*, *128*, e2022JB026148. https://doi.org/10.1029/2022JB026148

Received 28 NOV 2022
Accepted 31 JUL 2023

Author Contributions:

Conceptualization: Ana M. G. Ferreira
Formal analysis: William Sturgeon
Investigation: William Sturgeon
Methodology: Ana M. G. Ferreira, Lewis Schardong
Software: William Sturgeon, Augustin Marignier
Supervision: Ana M. G. Ferreira, Lewis Schardong
Visualization: William Sturgeon
Writing – original draft: William Sturgeon
Writing – review & editing: William Sturgeon, Ana M. G. Ferreira, Lewis Schardong, Augustin Marignier

Abstract Surface wave amplification measurements have narrower depth sensitivity when compared to more traditional seismic observables such as surface wave dispersion measurements. In particular, Love wave amplification measurements have the advantage of strong sensitivity to the crust. For the first time, we explore the potential of Love wave amplification measurements to image crustal velocity in the western U.S. The effects of overtone interference, radial anisotropy and Moho depth are all explored. Consequently, we present SWUS-crust, a three-dimensional shear-wave velocity model of crustal structure in the western U.S. We use Rayleigh wave amplification measurements in the period range of 38–114 s, along with Love wave amplification measurements in the period range of 38–62 s. We jointly invert over 6,400 multi-frequency measurements using the Monte-Carlo based Neighborhood Algorithm, which allows for uncertainty quantification. SWUS-crust confirms several features observed in previous models, such as high-velocity anomalies beneath the Columbia basin and low-velocity anomalies beneath the Basin and Range province. Certain features are sharpened in our model, such as the northern border of the High-Lava Plains in southern Oregon in the middle crust.

Plain Language Summary When an earthquake ruptures, seismic surface waves called Rayleigh and Love waves travel along the Earth's surface. Seismometers on the Earth's surface record ground motions caused by the passing seismic waves. The amplitude of these waves contains information about the local Earth structure beneath the station, from which we can produce images of the Earth's interior. Whilst Rayleigh waves have previously been used to image the Earth's upper mantle, this study uses Love waves for the first time. We explore how much information Love waves can provide and the advantages and limitations of using both Rayleigh and Love waves. Consequently, we build a new crustal model of the western U.S., called SWUS-crust. The model correlates with many well-known surface tectonic features, such as the Columbia Basin, Basin and Range province and Colorado Plateau. We also highlight certain features that have not been seen clearly in previous models, such as the High-Lava Plains in southern Oregon.

1. Introduction

Seismic imaging plays a crucial role in probing the structure and composition of the Earth's crust, especially when combined with laboratory measurements of crustal rocks (e.g., Christensen & Mooney, 1995; Rudnick & Gao, 2014). Seismic images of the Earth's crust are also useful for seismic hazard assessment (e.g., by providing key input information for accurate ground motion simulations) and are crucial for accurate earthquake source modeling (e.g., Frietsch et al., 2021). Moreover, removing the effects of the heterogeneous crust on seismic measurements can help constrain mantle structure (e.g., Ferreira et al., 2010; Schaeffer & Lebedev, 2015).

There are several global models of the crust, including CRUST1.0 (Laske et al., 2012), LITHO1.0 (Pasyanos et al., 2014) and the more recent model of Szwillus et al. (2019). These models constrain crustal seismic velocities on a $1° \times 1°$ grid scale and are mainly based on compilations of existing seismic and geophysical information, as well as on the modeling of seismic data. However, higher resolution models can be achieved on a regional scale. The dense network of EarthScope's USArray, which ended in 2021 (http://www.usarray.org/), provides an opportunity to image the local crust in finer detail across the continental U.S. (e.g., Porter et al., 2016; Schmandt & Humphreys, 2011). In particular, the western U.S. is an interesting study region due to its complex geological history and its wide range of tectonic provinces.

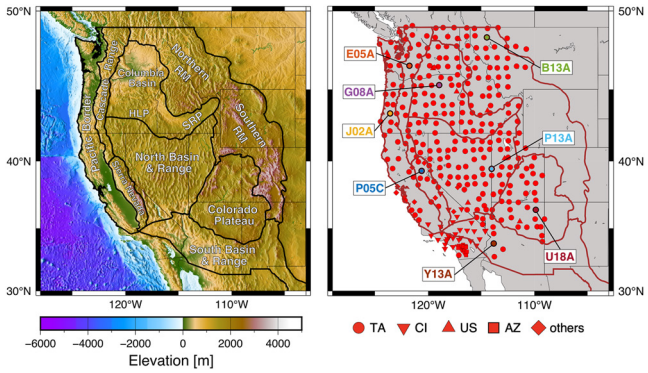

Figure 1. Left: Map of the western U.S., it's major tectonic provinces and other notable features, including the Rocky Mountains (RM), the Snake River Plain (SRP) and High Lava Plains (HLP). The elevation and bathymetry of the region are also plotted, according to ETOPO1. Right: the location of all 351 stations used in this study, with their network represented by different symbol types, as shown in the key. Other networks (diamond symbol) include BK, NN, IU, LB, and LI. For each major tectonic province we selected one illustrative station, which is labeled. These eight selected stations are used as illustrative examples throughout this study. The major tectonic provinces are delineated as solid brown lines.

Crustal thickening through tectonics across the western United States was largely controlled by the subduction of the Farallon plate in the late Mesozoic and Cenozoic (e.g., Schellart et al., 2010). Progressive subduction over the past >150 Ma caused major tectonic uplift and magmatism throughout the region (e.g., Humphreys & Coblentz, 2007). In the Cretaceous, subduction of the Farallon plate produced volcanism in the crust, eventually forming the Sierra Nevada batholith (Bateman & Eaton, 1967). Later, the Laramide orogeny is thought to have been responsible for crustal thickening and uplift of the Rocky Mountains range and of the Colorado Plateau in the east, which remains largely undeformed since the early Cenozoic compression and extension (e.g., Tesauro et al., 2014). Further north, subduction also formed the Cascade Mountain range through crustal thickening, which is home to a belt of Quaternary volcanoes above the Juan de Fuca plate subduction zone (Hildreth, 2007). In the Miocene, changes in the geometry of the Farallon slab led to extension and crustal thinning. The thinned crust of the North Basin and Range (Huber, 1981) produced low elevations across the area (e.g., Braile et al., 1989) and renewed volcanic activity (e.g., Stewart, 1980), but also increased elevations along the Sierra Nevada mountain range. Further north, intense magmatism about 17 Ma formed the Columbia Basin, a large igneous province caused by basaltic volcanism (e.g., Christiansen et al., 2002). Recent magmatism also marks the High Lava Plains (HLP in Figure 1) in south-eastern Oregon, the Snake River Plain (SRP in Figure 1) and the Yellowstone hotspot. Given such complex tectonic evolution, overall the western US shows a wide range of crustal structure, from thin crust in the Basin and Range (~25 km) and along the Pacific border (~20 km), to intermediate crustal thickness values in the Columbia Basin (~35 km) and thick crust beneath Rocky Mountains (~50 km) (Laske et al., 2013).

Many previous studies have utilized the large amount of available data from the USArray to image the crustal structure of the western U.S.. Surface wave ambient noise tomography has been one of the most widely used techniques to image shear-wave velocity in the crust (e.g., Bensen et al., 2009; Lin et al., 2008; Moschetti et al., 2007; Porter et al., 2016; Schmandt et al., 2015; Shapiro et al., 2005; Xie et al., 2018). In addition to ambient noise, receiver functions have also been commonly included to improve the depth-resolution of crustal layers (e.g., Chai et al., 2015; Schmandt et al., 2015; Shen et al., 2013). To further improve sensitivity to the crust, Rayleigh wave ellipticity measurements have also been included in more recent studies (e.g., Lin et al., 2014; Shen & Ritzwoller, 2016). Moreover, Pn waves (P waves trapped below the Moho) have also been used to constrain crustal and uppermost mantle structure in the U.S. For example, Buehler and Shearer (2012) used Pn measurements in the western US to estimate crustal thickness variations and velocity perturbations just below the Moho. More recently, Tesauro et al. (2014) used a variety of seismic data types, including Pn measurements, to constrain crustal depth, crustal P-wave velocity maps and Pn velocity maps beneath the U.S.

Another seismic observable that has recently received some attention is surface wave amplification, which carries information on how surface wave amplitudes change due to the local mantle and crustal structure at a given location (e.g., Eddy & Ekström, 2014). Recent studies have shown that surface wave amplification measurements have the potential for higher-resolution imaging when compared to surface wave dispersion measurements (e.g., Eddy & Ekström, 2014; Schardong et al., 2019). Surface wave amplification has been measured in a few studies. Taylor et al. (2009) measured site amplification factors using ambient noise in California using a standing-wave methodology. Later, Lin et al. (2012) measured receiver-side amplification across the USArray using fundamental mode Rayleigh waves with a method similar to Eikonal and Helmholtz tomography. Eddy and Ekström (2014) developed a novel method to measure local amplification using amplitude ratios at nearby stations, which we will discuss in more detail later in this study. Schardong et al. (2019) built upon the methodology of Eddy and Ekström (2014) to generate a new data set of amplification measurements across the western U.S. for vertical- and horizontal-component Rayleigh waves and Love waves in the period range between $T \sim 38$ s and $T \sim 114$ s. This study was the first to invert amplification measurements for crustal and mantle shear-wave velocity structure in the western U.S. The resulting model, SWUS-amp, used vertical-component Rayleigh wave amplification measurements to constrain mantle shear-wave velocity down to ~300 km depth. However, the crust was only

parameterized using a single layer between the Moho and surface since the data used could not constrain more complex crustal models (Figure S1 in the Supporting Information S1).

In this study we combine Love and Rayleigh wave amplification measurements to constrain crustal shear-wave velocity in the western U.S.. Love waves have a particularly strong sensitivity to crustal structure, which is explored in this work. The Love wave measurements are jointly inverted with Rayleigh wave amplification measurements to build 1-D shear-wave velocity models beneath each considered station in the western USArray. Then, these 1-D profiles are interpolated to build a new 3-D shear-wave speed model of the crust, SWUS-crust. Finally, we interpret the features imaged in SWUS-crust and compare them to those reported in other recent studies.

2. Surface Wave Amplification Measurements

2.1. Seismic Data

We use fundamental-mode vertical-component Rayleigh (hereafter referred simply as Rayleigh waves) and Love wave amplitude anomalies. Both datasets were measured using the mode-branch stripping technique (van Heijst & Woodhouse, 1997). The Rayleigh wave data set has also been used in global studies of attenuation (Bao et al., 2016; Dalton et al., 2017) and in the study of Schardong et al. (2019), which determined crustal and upper mantle shear-wave velocity beneath the western U.S.. This data set contains data from the Transportable Array, which was part of the larger USArray between 2004 and 2007. The data set is based on 7,744 earthquakes with $M > 5.0$ that occurred in 2004–2007, recorded at 351 stations in the western U.S.. Figure 1 shows the locations of the stations used in this study and their networks. Rayleigh waves are measured at 12 dominant periods between $T \sim 38$–114 s, whereas Love waves are measured at seven dominant periods between $T \sim 38$–62 s. We choose to include only shorter-period Love wave measurements ($T \leq 62$ s), which have stronger sensitivity to the crust, as can be seen in Figure S2 in the Supporting Information S1. We performed inversions using longer-period Love waves (T ~ 69–113 s), which resulted in very similar 1-D shear-wave speed (v_S) profiles in the crust, thus not affecting the results of this study, but they occasionally led to less stable inversions likely due to noisier measurements. Our measurement procedure provides a total of 6,423 multi-frequency, surface-wave amplification measurements used in this study.

2.2. Measurement Technique

We use Rayleigh and Love wave amplification measurements obtained with the measurement technique developed by Schardong et al. (2019), which is briefly summarized in this section. The local frequency-dependent amplification of surface waves at a given receiver, R, is theoretically expressed by (e.g., Ferreira & Woodhouse, 2007):

$$A_R(\omega) = \frac{Y(\omega)}{Y_0(\omega)} \sqrt{\frac{C_g^0(\omega)}{C_g(\omega)}}, \tag{1}$$

where $Y(\omega)$ is the local displacement eigen function of the Earth's normal mode equivalent to the surface wave considered at a given frequency ω. $Y(\omega)$ corresponds to the vertical component eigen function $U(\omega)$ for Rayleigh waves, and to the transverse component eigen function $W(\omega)$ for Love waves. $C_g(\omega)$ is the local group velocity which is measured from spheroidal and toroidal modes for Rayleigh and Love waves, respectively. $Y_0(\omega)$ and $C_g^0(\omega)$ are the corresponding eigen function and group velocity, respectively, computed for the 1-D reference model PREM (Dziewonski & Anderson, 1981). The eigen functions and group velocities are calculated using a normal mode formalism (F. Gilbert, 1971) and using the software package Mineos 1.0.2 (Masters et al., 2011).

In addition to the amplification (or receiver) contribution $A_R(\omega)$, observed surface wave amplitudes are also affected by source and path effects. Eddy and Ekström (2014) developed a method to remove the contribution from the source and path by averaging ratios of amplitudes between pairs of nearby stations i and j, which is ideally suited to dense seismic networks such as the USArray. Local amplification, $d_{ij}^k(\omega)$, is calculated by taking the ratios of surface-wave amplitudes for a given earthquake, k:

$$d_{ij}^k(\omega) = \ln(A_i(\omega)/A_j(\omega)) = \ln(A_i(\omega)) - \ln(A_j(\omega)) \tag{2}$$

followed by an average taken over all the earthquakes considered. Schardong et al. (2019) followed the same approach, but with some minor modifications considering an azimuthal weighting of the earthquakes,

$$\bar{d}_{ij}(\omega) = \frac{\sum_{k=1}^{N_E} d_{ij}^k w^k}{\sum_{k=1}^{N_E} w^k} \tag{3}$$

The azimuthal weighting coefficient is given by $w^k = 1 - n_E/N_E$, where n_E is the number of earthquakes located in an azimuthal bin of 15°, for each earthquake k, and N_E is the number of common earthquakes recorded at stations i and j. We then calculate the corresponding weighted standard deviation using:

$$\sigma_{ij}(\omega) = \sqrt{\frac{\sum_{k=1}^{N_E} w^k \left(d_{ij}^k(\omega) - \bar{d}_{ij}(\omega)\right)^2}{\frac{N_E - 1}{N_E} \sum_{k=1}^{N_E} w^k}} \tag{4}$$

We then invert the average inter-station frequency-dependent measurements for local amplification factors at each station ($A_{R,i}$ and $A_{R,j}$). Adopting a least squares inversion approach, we minimize the misfit function:

$$m^2 = \sum_{ij} \frac{1}{\sigma_{ij}^2} \left[\left(\ln(A_{R,i}(\omega)) - \ln(A_{R,j}(\omega)) - \bar{d}_{ij}(\omega)\right)\right]^2 \tag{5}$$

To constrain the inversion, Schardong et al. (2019) imposed the condition that the sum of the amplification factors must equal the sum of the theoretical amplification factors (Equation 1), calculated using SGLOBE-rani (Chang et al., 2015) for mantle structure combined with CRUST2.0 (Bassin, 2000) for crustal structure. The choice of model was extensively investigated by Schardong et al. (2019).

It was noted in Schardong et al. (2019) that the amplification values obtained with distinct amplification sum constraints vary significantly, which would lead to distinct absolute v_S values when inverting the amplification measurements. Therefore, absolute values of v_S will not be interpreted in this study. However, it was found that inverted v_S perturbations did not strongly depend on the imposed sum of the amplification factors, therefore our model can be interpreted in terms of v_S perturbations.

Inter-station measurement uncertainties, $\underline{\mathbf{e}}_R$, are calculated at all stations and available periods using:

$$\underline{\mathbf{e}}_R = \sqrt{\mathrm{diag}\left(\underline{\underline{\mathbf{P}}}^{-1} \cdot \underline{\underline{\mathbf{S}}} \cdot \left(\underline{\underline{\mathbf{P}}}^{-1}\right)^{\mathrm{T}}\right)} \tag{6}$$

where the $\mathbf{P}$ matrix relates $\ln(A_{R,i}(\omega)) - \ln(A_{R,j}(\omega))$ with $d_{ij}(\omega)$ (Equation 5) and $\underline{\underline{\mathbf{S}}}$ a diagonal matrix containing observed data uncertainties in the form of weighted standard deviations (Equation 4). These errors cannot be directly compared to previous studies (e.g., Eddy & Ekström, 2014; Lin et al., 2012) because of different data error definitions used.

We also apply selection criteria on our amplification curves in order to remove all outliers, for both Rayleigh and Love waves. Specific details are given in the supplementary information of Schardong et al. (2019), and here we briefly summarize them. As shown in Figure S3 in the Supporting Information S1, we ensure that we only consider amplification factors for which five or more inter-station measurements are available. We ensure there is a good azimuthal coverage of stations around our primary station, in order to avoid azimuthal biases leaking into our inter-station amplification measurements. Specifically, we remove all stations with an azimuthal completeness coefficient of less than 20% (as defined by Equation 2 in the SI of Schardong et al., 2019). Outliers due to geographical coherency are removed by ensuring amplification factors for each station do not vary by more than 2.5σ compared to all nearby stations, where σ is the standard deviation of the amplification values of all nearby stations. Lastly, we remove all stations with a propagated error greater than 0.1, as given by Equation 6. This threshold value ensured obvious outliers were removed, whilst keeping the bulk amount of data available. The strict outlier analysis is performed to focus on the highest quality signals that can be modeled with our approach. As a result, wavefield complexities such as multipathing, off-circle-propagation, arrival angle deviations (for both Love and Rayleigh waves) and focusing/defocusing will not bias the resultant amplification measurements.

Another issue that can affect the quality of surface wave amplification measurements is overtone interference (e.g., Hariharan et al., 2020, 2022). Interference along the ray path depends largely on epicentral distance, group velocity, source depth and the source mechanism. In Figure S4 in the Supporting Information S1 we plot group velocity against period for Rayleigh and Loves waves, for two example models in the western U.S. which show a

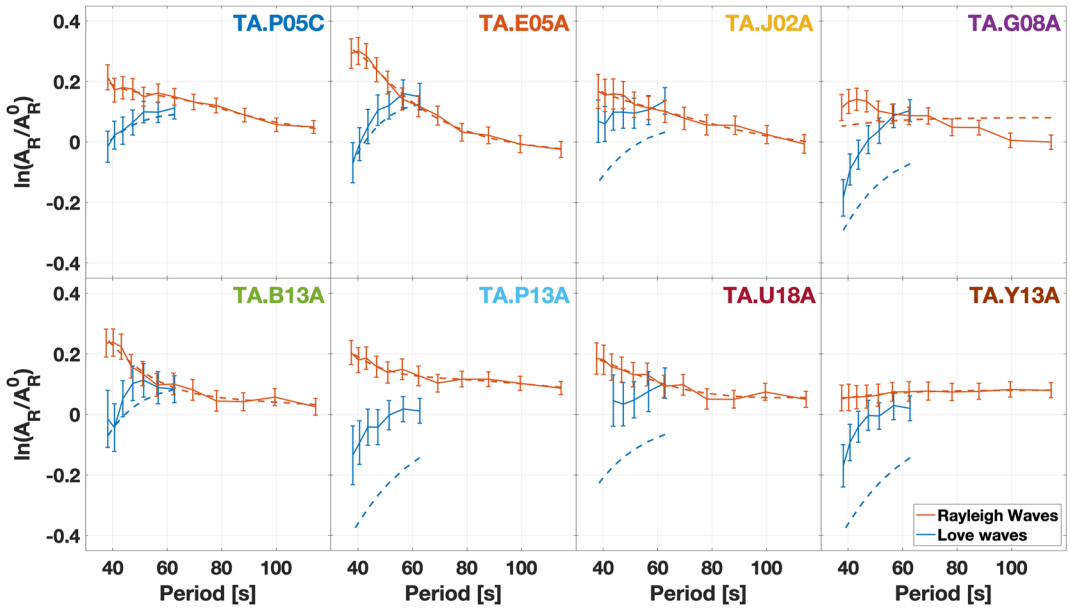

Figure 2. Comparisons of measured (solid lines with error bars) and theoretical amplification curves (dashed lines), calculated using 1-D profiles from SWUS-amp Schardong et al. (2019). Each illustrative station, given in the top-right of each panel, resides in a different major tectonic province (see Figure 1). Amplification curves for Rayleigh waves are shown in red, while for Love waves are shown in blue.

range of crustal thicknesses and upper mantle structure (TA.Y13A and TA.U18A from SWUS-amp; Schardong et al., 2019). Rayleigh wave group velocity curves show a clear separation between the fundamental mode and overtones. In addition, our Rayleigh wave data set is dominated by paths with epicentral distances <120°, at which distances the effect of overtone interference is significantly less pronounced, as shown in Hariharan et al. (2020, 2022). The distribution of our Rayleigh wave epicentral distances used in Rayleigh wave data set can be seen in Figure S5 in the Supporting Information S1. However, Love waves show potential contamination between the fundamental mode and first overtone at the period range considered in this study, $T \sim 38$–62 s. As a result, we calculate Love wave excitation ratios between the fundamental mode and the first overtone. We use PREM as our Earth model and use source depths and focal mechanisms for the events used in our study from the GCMT catalog. Our analysis shows that 81% of measurements have an excitation ratio <0.5. Whilst this shows that there is a possibility for some interference, for the vast majority of measurements the fundamental mode will be strongly dominant.

In this study we perform inversions of inter-station amplification measurements from 432 stations in the western U.S., which have both Rayleigh and Love amplification data. Following these inversions, we removed stations for which the inversions had a data misfit larger than 20 (Equation 7). Moreover, we visually examined all the stations and removed those that showed rough (i.e., non-smooth) or irregular amplification curves that could not be matched in the inversions. As a result, we kept a total of 351 stations and are still left with a good distribution of stations across the region (Figure 1).

2.3. Results

Figure 2 shows illustrative examples of observed amplification curves for Rayleigh and Love waves compared to theoretical predictions using the 1-D depth profiles from SWUS-amp (Schardong et al., 2019). Each station resides in a different major tectonic province (Figure 1), in order to show the range of amplification curves available in the western U.S. Given that SWUS-amp was built using the same Rayleigh wave data set as in this study, the fit between the theoretical and observed Rayleigh wave amplification curves is excellent. However, the Love wave theoretical curves show a range of data fits. Whilst stations TA.P05C and TA.E05A show reasonable data fits, other stations show very poor fit, such as TA.U18A and TA.Y13A. Given the strong sensitivity of

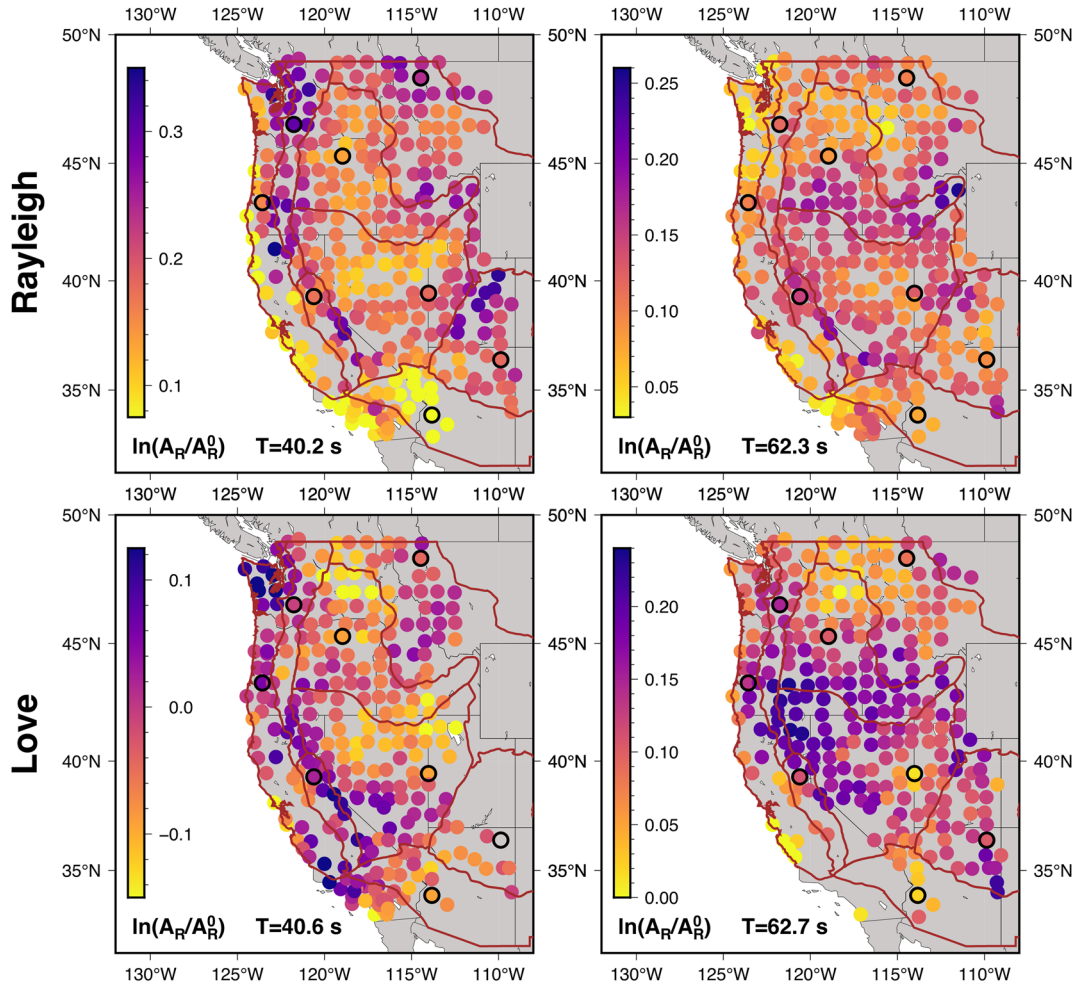

Figure 3. Top row: Rayleigh wave amplification measurements at T ~ 40 s (left) and T ~ 62 s (right). Bottom row: Love wave amplification measurements at T ~ 41 s (left) and T ~ 63 s (right). The eight illustrative stations shown in Figure 1 are highlighted with black borders. Brown lines outline the major tectonic provinces.

Love waves to the crust, as can be seen in Figure S2 in the Supporting Information S1, this suggests that using Love wave amplification may help to constrain a more detailed crustal model than in SWUS-amp.

Figure 3 shows the local amplification measurements obtained for the available stations at wave periods of $T \sim 40$ s and $T \sim 62$ s. The Rayleigh and Love wave amplification maps look different to one another because of their distinct sensitivities, however there are also some common features. At $T \sim 40$ s for Rayleigh waves, low-local amplification is retrieved in the South Basin and Range and along the Pacific coastline. Conversely, high amplifying structures are retrieved along the Sierra Nevada and Cascade ranges, and at the northeastern edge of the Colorado Plateau. At $T \sim 62$ s, high amplification is imaged along the southern Columbia Basin and Snake River Plain. This is in contrast with the low-amplifying structures in the along the Pacific border, the North Rocky Mountain and in the northernmost part of the Columbia Basin (see Figure 1 for the geographical location of these regions).

At $T \sim 40$ s for Love waves, we observe low-amplifying structures beneath the Columbia Basin and northeastern Basin and Range. Highly amplifying structures are observed along the northern Pacific coast and the western border of the North Basin and Range. At $T \sim 62$ s, there are highly amplifying structures across the North Basin and Range, the Cascade Range and the southern Columbia Basin. This is in contrast to the northern Columbia Basin, Northern Rockies and southern Pacific border.

Previous studies have shown that local Rayleigh wave amplification shows a correlation with crustal thickness (Eddy & Ekström, 2014; Gilbert, 2012). We observe a similar pattern in Figure 3, where the thick crust beneath

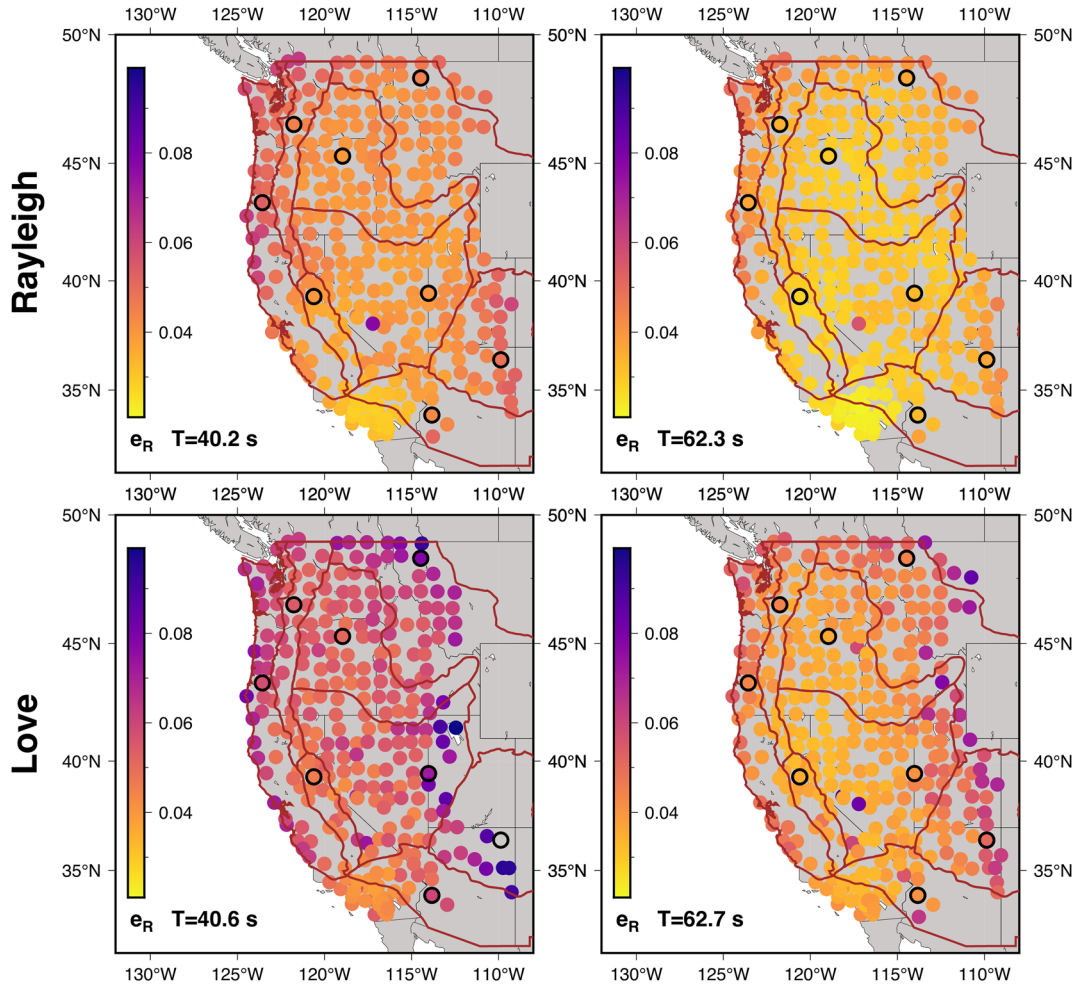

Figure 4. Top row: Rayleigh wave amplification error measurements at $T \sim 40$ s (left) and $T \sim 62$ s (right). Bottom row: Love wave amplification error measurements at $T \sim 41$ s (left) and $T \sim 63$ s (right). The eight illustrative stations are highlighted with black borders. The major tectonic provinces are outlined in solid brown lines.

the Sierra Nevada Mountains, Northern Rocky Mountains and Snake River Plain shows high-amplification, whereas the thinner crust beneath the Columbia Basin, North and South Basin and Range and Pacific coast shows low-amplification. Likewise, the Love wave amplification maps show a similar correlation to crustal thickness.

The propagated amplification errors (Equation 6) can be seen for each station in Figure 4, for the same illustrative wave periods. For both Rayleigh and Love wave amplification error maps, the errors are largest around the edges. The reason for this is because the number of stations pairs is lower for the outer stations (see Figure S3a in the Supporting Information S1), and consequently the azimuthal coverage of station pairs is also lower (Figure S3b in the Supporting Information S1). Propagated errors are greater for Love waves because in general horizontal component data are noisier than vertical component data.

3. Inverting Surface Wave Amplification for Crustal Shear Wave Speed

3.1. Inversion Method

There is a non-linear relation between surface-wave amplification and Earth structure. We therefore use the fully non-linear Neighborhood Algorithm (NA; Sambridge, 1999) to jointly invert the observed amplification curves for depth-dependent v_S beneath each available station. The NA is a Monte Carlo based approach that divides the parameter space into Voronoi cells (Voronoï, 1908) to quickly find an ensemble of models that best fit the data. The NA has been used to constrain crustal structure in a number of different settings, including in the western

U.S. (e.g., Moschetti et al., 2010b), Portugal (Attanayake et al., 2017), northern Italy (Berbellini et al., 2017), the Azores (Ferreira et al., 2020), central Java (Ariyanto et al., 2018), the Netherlands (Yudistira et al., 2017) and Greenland (Jones et al., 2021). The NA is composed of two main stages. First, the NA randomly samples the parameter space and each model is ranked according to its misfit between the observed and theoretical amplification curves. Second, the NA enters an optimisation stage where in each iteration models are sampled within the neighborhood of the best-fitting models. After extensive testing, in the initial stage we choose to sample 2,000 random models. Then, in the second stage, for each iteration the NA picks 20 models within the neighborhood of the best five models from the previous iteration. Moreover, the NA proceeds for 500 iterations to ensure the solution converges on the same model each time. Figure S6 in the Supporting Information S1 shows an example of misfit evolution, clearly showing good convergence.

We use a L_2-norm misfit function:

$$s(\mathbf{m}) = \sum_{i=1}^{N} \frac{(A_{R,i} - g_i(\mathbf{m}))^2}{e_{R,i}^2} \tag{7}$$

where $g_i(\mathbf{m})$ is the predicted amplification for the model $\mathbf{m}$ being sampled, $A_{R,i}$ is the observed amplification, $e_{R,i}$ is the observed error, N is the number of wave periods and i is the individual wave period.

Given that crustal layers typically have strong contrasts in seismic properties and the success of previous studies in using layered parameterizations for the crust, notably with three layers (e.g., Ferreira et al., 2020; Laske et al., 2012; Schmandt et al., 2015), we decided to also use a three-layered crustal parameterization. Since our mantle model SWUS-amp (Schardong et al., 2019) was successfully built using Moho depths from CRUST1.0, we also constrain the depths of our three-layer crustal model using CRUST1.0 (Figure S7 in the Supporting Information S1). We also note that our amplification measurements do not have the sensitivity to resolve layer thickness. We choose not to invert for sediment layers, as that would require shorter period amplification measurements.

One of the advantages of using the NA is that it provides an ensemble of models that can be used to estimate uncertainties for our final solution. We calculate the percentual uncertainty e_{v_s} for each station used to build our model by considering the range of velocities, $v_{s,\max} - v_{s,\min}$, of all models within a 20% misfit of the best-fitting model, $v_{s,\text{best}}$, in each crustal layer.

$$e_{v_s} = \frac{(v_{s,\max} - v_{s,\min})}{v_{s,\text{best}}} \times 100 \tag{8}$$

We choose a threshold of 20% because it includes models that fit the amplification curves reasonably well. A looser threshold would include models with a poor data fit, and a stricter threshold would not be representative of the range of models that fit the data relatively well.

We invert for v_S whilst scaling for v_P and ρ using the general Brocher relation (Brocher, 2005). The mantle structure is fixed to that of SWUS-amp (Schardong et al., 2019) between the Moho and ~300 km depth and to PREM beneath this depth. In the next section we will justify this choice of mantle model with the help of synthetic inversion tests and trade-off tests between crustal and mantle structure. Constraints are imposed on the inversion whereby v_S must increase with depth within each crustal layer as well as beneath the Moho. Previous crustal models in the western U.S. show that v_S always increases with depth within these ranges (e.g., Schmandt et al., 2015; Shen & Ritzwoller, 2016) and our inversion tests showed that these constraints help stabilize the inversions. We invert for shear-wave velocity perturbations $\left(\frac{\delta v_S}{v_S}\right)$, with respect to the average crustal v_S of PREM. In order to search a wide range of possible model parameters, we allow the inversion to search between ±40% of the average crustal v_S of PREM in each layer.

3.2. Synthetic Inversion Tests

We perform synthetic inversion tests to investigate how capable our inversion method is of retrieving realistic input crustal models. We use the isotropic model of Moschetti et al. (2010b) as our input model with the sediment layer removed. Gaussian random noise is added to each synthetic data point by simulating 200 predicted amplification curves using the standard deviations of the real data measurements. The average amplification curve and standard deviation of these simulated curves are used as the input synthetic data into the NA as described in Section 3.1.

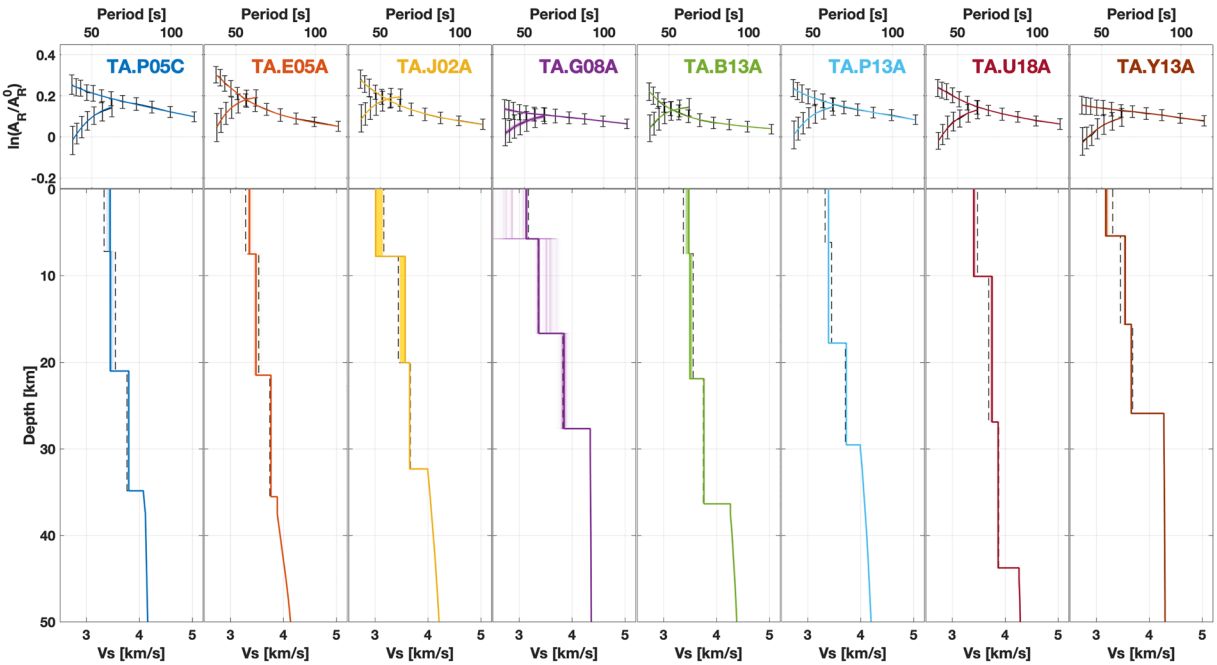

Figure 5. Example of results from synthetic inversion tests. Top row: amplification curves computed for synthetic input 1-D v_S profiles (black lines with error bars) and the retrieved output 1-D v_S profiles (colored lines). The curves with longer periods are for Rayleigh waves, and the shorter curves are for Love waves. Bottom row: Corresponding input (black dashed lines) and output (bold colored lines) v_S models. The more transparent colored lines show the models with misfit values within 20% of the model with the lowest misfit.

Figure 5 shows the results from synthetic inversions for our 8 stations of interest. Overall, the synthetic inversions work very well, showing that the NA converges to the input model even with noise introduced. Models within a 20% misfit of the best retrieved model are shown by colored lines and it is encouraging to see that these models show a small range in velocities, centered around the best-fitting model. There are, however, some slightly imperfect solutions which are due to trade-offs in v_S between the crustal layers (e.g., for stations TA.J02A and TA.G08A).

We also ran a number of synthetic tests to verify if the addition of Love wave amplification data helps to further constrain crustal and mantle v_S compared to using Rayleigh wave amplification data alone. Our extensive testing revealed that due to their strong sensitivity to the crust, they could not constrain the mantle. Regarding the benefit for crustal imaging, Figure S8 in the Supporting Information S1 shows an example of a synthetic inversion where the input model is an isotropic model from Moschetti et al. (2010b) located in the Columbia Basin. We show the model retrieval when only inverting Rayleigh wave data (left panel) compared to jointly inverting Rayleigh and Love wave data (right panel). As expected, model retrieval is significantly improved with the incorporation of Love wave measurements due to their strong sensitivity to crustal depths.

Next, due to Love wave amplification being mainly sensitive to v_{SH}, we performed joint inversions of Rayleigh and Love wave amplification data for a radially anisotropic crust. However, the increased number of parameters that needed to be inverted for with a relatively small data set led to unstable inversions. This supports our choice of inverting only for an isotropic crust. Moschetti et al. (2010b) identified areas of strong crustal radial anisotropy in the western U.S. In order to examine the effect of radial anisotropy on our inversions, we performed additional synthetic inversion tests whereby the input model is radially anisotropic but we inverted only for isotropic crustal structure following our usual inversion procedure. We found that either (a) we could not fit both Rayleigh and Love wave data well (Figure S9 in the Supporting Information S1), or (b) we could fit both Rayleigh and Love wave data well but the model was close to the input Voigt average model.

In order to investigate model parameter trade-offs in our inversions further, we produce trade-off plots by plotting all the crustal and mantle model parameters used in the inversions against each other (see e.g., Figure S10 in the Supporting Information S1 for station TA.Y13A). Furthermore, we perform inversions inverting not only for the three crustal layers but also for the v_S coefficients of one spline function describing the uppermost mantle

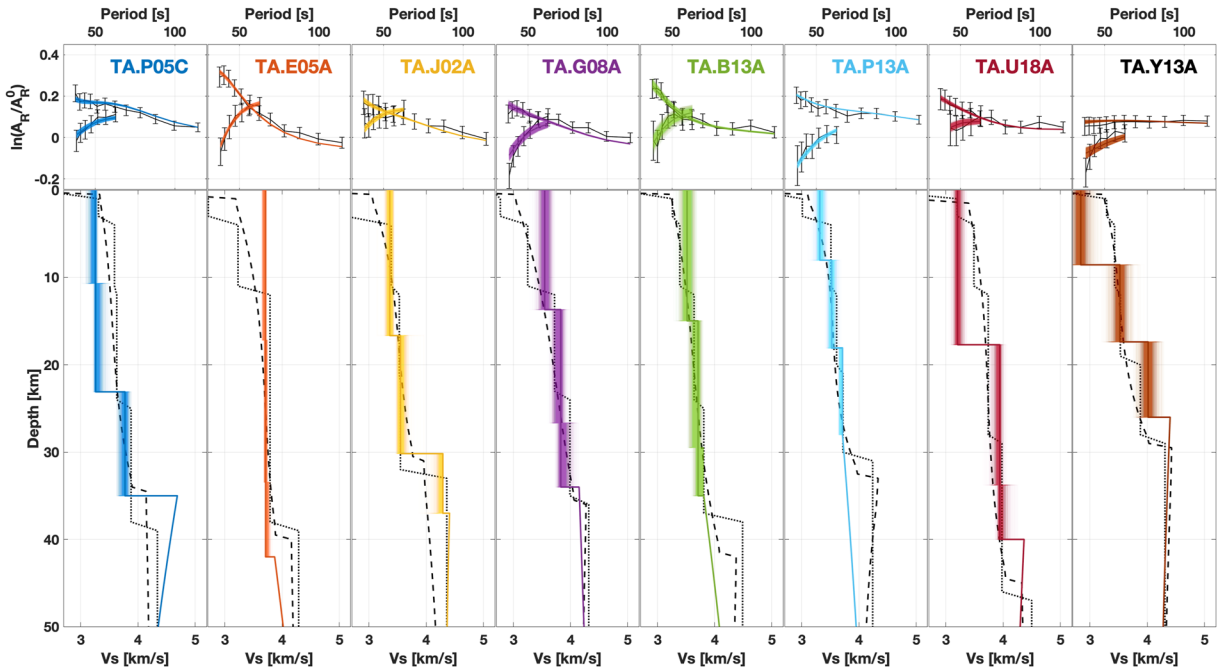

Figure 6. Real data inversions for depth-dependent v_S for the eight example stations located in each major tectonic province in the western U.S. (see Figure 1). Top row: Amplification curves for Rayleigh waves (long curves) and Love waves (short curves) for real data (black lines with error bars), the best retrieved model (thick colored lines) and models within a 20% misfit value of the best-fitting model (thin colored lines). Bottom row: 1-D shear-velocity crustal profiles for SWUS-crust (colored lines), compared to the models of Schmandt et al. (2015) (dotted lines) and Shen and Ritzwoller (2016) (dashed lines).

structure between the Moho and ~90 km depth. This ensures that we are not biasing our crustal model by fixing the mantle to SWUS-amp. Figure S10 in the Supporting Information S1 in the supplementary information shows that there is a small trade-off in v_S between the uppermost mantle and lower crust, indicating that fixing v_S in the mantle does not significantly affect the retrieved crustal model. This also highlights the fact that Love waves have low sensitivity to the uppermost mantle, but add important sensitivity to the crust, as can be seen by the sharp gradient in sensitivity in Figure S2 in the Supporting Information S1. Conversely, Rayleigh waves show strong sensitivity to the crust and uppermost mantle, but, as found by Schardong et al. (2019), they cannot constrain alone crustal models more complex than a single layer.

We also ran a number of synthetic inversion tests to investigate the effect of not including a sediment layer in our inversions. We use the isotropic model of Moschetti et al. (2010b) in the Columbia Basin as the input model for our synthetic inversion tests. Figure S11 in the Supporting Information S1 shows two cases where we (a) invert for only crustal structure and the model retrieval is excellent; (b) The input model has a sediment layer, but the inversion does not account for it. The model retrieval is poor compared to Case 1, with the retrieved v_S in the upper crustal layer being about the average of v_S in the sediment and sub-sediment layers in the input model (despite different layer thicknesses). Hence, this test shows in a quantitative way that in some regions of the model the velocity in the upper layer in our models could be a mix of sediments and deeper structures. However, this synthetic test also reveals that the presence of sediments may also lead to a trade-off in v_S between the upper and middle crustal layers. This has also occasionally been seen in other synthetic tests, such as for station TA.Y13A in Figure 5.

3.3. Results From Real Data Inversions

We jointly invert Rayleigh and Love wave amplification curves for 1-D v_S profiles using the NA as described in Section 3.1. Figure 6 shows examples of 1-D v_S profiles obtained for the eight illustrative stations located within each major tectonic province in the western U.S considered in this study. For reference, we compare our model with the layered crustal model of Schmandt et al. (2015) and the smooth crustal model of Shen and Ritzwoller (2016), which were built using completely independent data sets from this study. As with the synthetic profiles in Figure 5, we plot all models with a data misfit within 20% of the best-fitting model. These models are clustered around the best-fitting model, showing that we have a well-converged solution and that any trade-offs

apparent in the model do not have a significant impact on our final model. Figure S6 in the Supporting Information S1 shows an illustrative example of convergence of an inversion for station TA.P13A. It can be seen that convergence is achieved after 10,000 models but we continue the inversion up to 12,000 models for insurance.

We compare SWUS-crust to the single crustal layer of SWUS-amp (Figure S1 in the Supporting Information S1) to further check if our modeling is biased by the presence of anisotropy. Similar crustal features are seen in SWUS-amp compared to SWUS-crust, for example, high v_S beneath the Columbia basin, Colorado Plateau and Northern Rocky mountains. Similarly, low v_S is observed beneath parts of the Northern Basin and Range and the High Lava Plains. Such similarities suggest that the inclusion of Love wave amplification data in SWUS-amp has not introduced a bias due, for example, to radial anisotropy. Furthermore, as mentioned previously, SWUS-amp does not fit Love wave data well, as seen in Figure 2. As explained previously, We ran several anisotropic and isotropic inversions including Love waves and whilst isotropic inversions remained robust, anisotropic inversions were not. The data fit for both Rayleigh and Love waves is good, but is not always perfect, indicating that a small amount of anisotropy could be present, and indicating no clear bias. Future robust modeling of crustal anisotropy requires the inclusion of further data types such as, for example, ambient noise dispersion data.

There are similarities and differences between the various 1-D v_S profiles. We notice that our results obtained for the lower- and mid-crustal layer match the other models well, but there are some differences in the upper-crustal layer. In some profiles we observe higher upper-crustal v_S values (e.g., for stations TA. E05A, TA.G08A) and in other cases we observe lower upper-crustal v_S (e.g., TA.U18A, TA.Y13A). The geographical differences in the velocities and the model uncertainties will be discussed in detail in the next section.

The 1-D v_S profiles are interpolated laterally for each layer using an ordinary kriging routine to obtain a new 3-D crustal model in the western U.S. This technique was successfully used in previous imaging studies (e.g., Berbellini et al., 2017; Jones et al., 2021; Schardong et al., 2019), as the technique allows for interpolation of sparse or irregularly sampled data.

In order to estimate the spatial covariance amongst our stations, we first constructed a semi-variogram. This quantifies the degree of variability in the inferred velocities as a function of the separation distance. A "spherical model" is used to quantify the increase in variability with increased separation distance. The extracted parameters from the semi-variogram describing how the velocities at stations covary with separation distance are used to model the covariance between velocities at stations and velocities across a uniform grid.

We explore a range of models to fit the semi-variogram (e.g., in the upper crustal layer, Figure S12 in the Supporting Information S1), and choose a spherical model as it both fits the semi-variogram well and shows relatively low interpolation uncertainty. We note that, as expected, uncertainties in the interpolated values decrease in areas with high station coverage. Figure 7 shows the model before and after interpolating the profiles. We refer to the resulting model as SWUS-crust, whose key features will be discussed in the next section. For completeness, we also show SWUS-amp in terms of absolute v_S in Figure S13 in the Supporting Information S1.

Figure 7 also shows the uncertainty of our real data inversions in each crustal layer, as defined by Equation 8. There appears to be a relation between crustal thickness and model uncertainty, whereby the regions of thinnest crust (e.g., North and South Basin and Range, Pacific Coast) have the highest uncertainty. The crustal thickness in CRUST1.0, in general, is shallower than in Shen and Ritzwoller (2016), who used receiver functions to help constrain the Moho depth, as can be seen in Figures 5 and 6. As a result, we re-ran our inversions changing the Moho depth to that defined by Shen and Ritzwoller (2016) for four stations in the North Basin and Range, as seen in Figure S14 in the Supporting Information S1. Uncertainty in the lower crust decreased by ~3%, which is not very substantial. This suggests that uncertainties in Moho depth defined by CRUST1.0 do not significantly affect the uncertainty in our model. Model uncertainties in the upper crust are generally higher compared to the middle and lower crust. This is likely due to the fact that we do not invert very short period data, which would be most sensitive to upper crustal depths.

We also re-emphasize that the choice of model used as the amplification sum constraint, as discussed in Section 2.2, is a possible source of uncertainty affecting the v_S perturbations in SWUS-crust and the associated uncertainty maps.

4. Discussion

Previous studies of the crustal structure of the western U.S. have used various combinations of data, including surface wave dispersion data from both seismic ambient noise and teleseismic events, Rayleigh wave ellipticity measurements and receiver functions. In this proof-of-concept study, we built the first crustal model based on

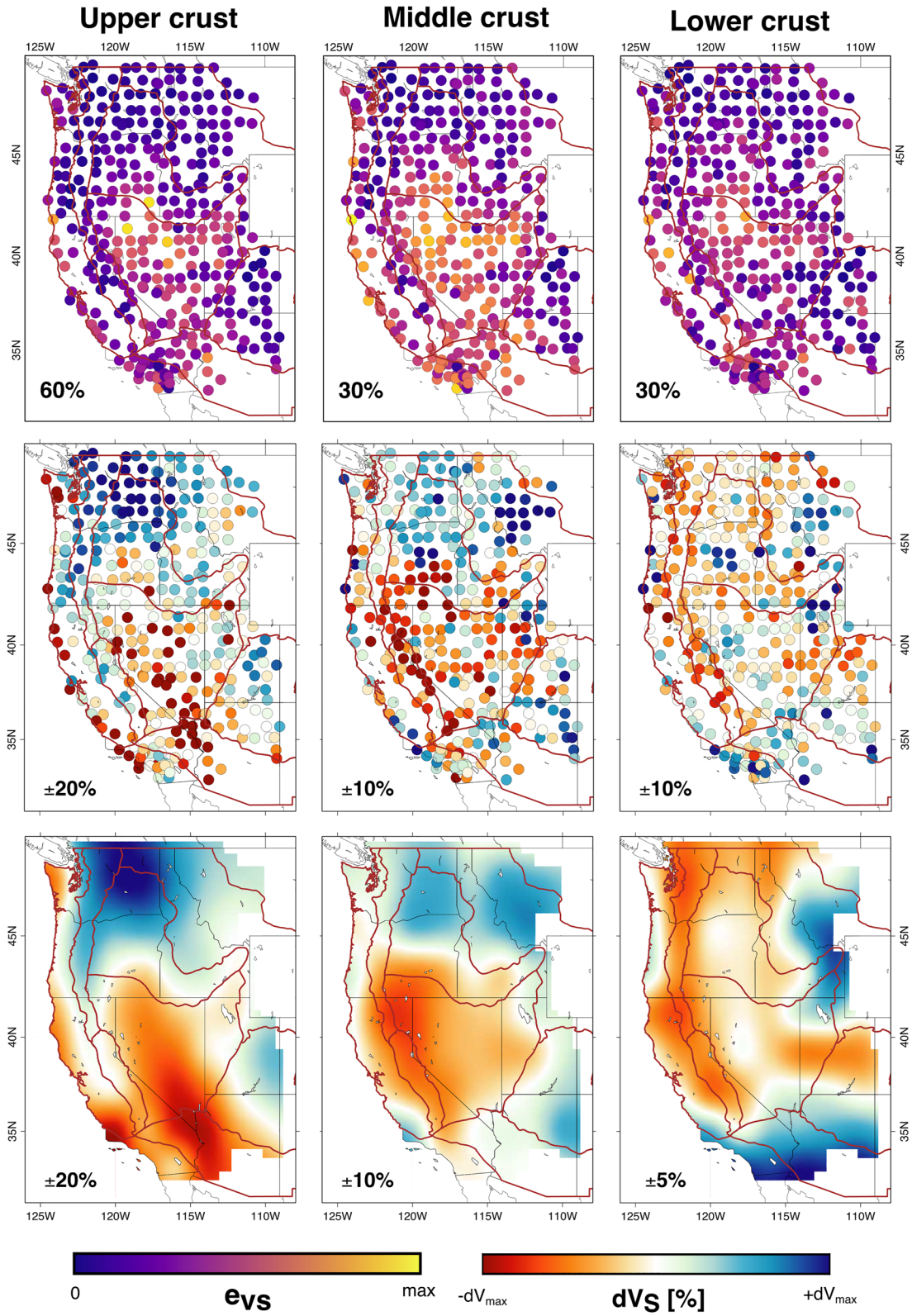

Figure 7. Tow row: Maps of percentual model uncertainties, as defined by Equation 8, for each station used in the construction of SWUS-crust. The maximum of the scale bar is indicated in the bottom left of each panel. Middle row: Deviations from the average v_s in each layer, in the upper, middle and lower crust at each station for our model SWUS-crust. Bottom row: the same as the top row but after kriging interpolation (see text for further details).

Rayleigh and Love amplification data alone with wave periods $T > 38$ s. As shown by the synthetic tests presented in Section 3.2, the narrow depth sensitivity of these observables (Figure S2 in the Supporting Information S1) enables the construction of our new detailed crustal model of the western U.S., SWUS-crust. We remind the reader that there may be trade-offs in v_S structure in the upper and middle crustal layers due to the choice of parameterization and the presence of unmodelled sediments in certain regions.

4.1. Comparison With Other Models

Table S1 in the Supporting Information S1 provides details on the data sets, parameterization, forward modeling, inversion methods and constraints used by other models discussed in this study; Chai et al. (2015); Laske et al. (2012); Moschetti et al. (2010b); Porter et al. (2016); Schmandt et al. (2015); Shen and Ritzwoller (2016); Xie et al. (2018).

Figure 8 compares SWUS-crust with other crustal layered models of the western U.S., including the global crustal model CRUST1.0 (Laske et al., 2012), the regional models of Moschetti et al. (2010b) and Schmandt et al. (2015). Whilst we do not invert for sedimentary layers, we choose to show them for the other models to aid our interpretation, since the upper crust layer of SWUS-crust may also reflect shallower sedimentary structures. In addition to these models, we also compare SWUS-crust to a number of smoothly parameterized crustal models at depth intervals of 10 km, (Figure S15 in the Supporting Information S1) Porter et al. (2016); Shen and Ritzwoller (2016); Xie et al. (2018) and intervals of 5 km for further models in Figure S16 (Chai et al., 2015).

Figures 7 and 8 show that there are some similarities between the different models, notably between the models with a layered parameterization shown in Figure 8, which show for example, mostly low crustal v_S anomalies along the Pacific coast in the upper crust and high crustal v_S anomalies beneath the Columbia basin in the middle crust. On the other hand, there are also considerable differences between the models, notably regarding their small scale structures. For example, SWUS-crust shows a lot of regional variations compared to CRUST1.0 (Figure 8) and the model of Chai et al. (2015) (Figure S16 in the Supporting Information S1), while other models show more comparable small-scale heterogeneity.

4.2. SWUS-Crust Model Features

Figure 8 shows that the signature of the Columbia basin in SWUS-crust is a high v_S anomaly throughout the upper and middle crust, with its magnitude decreasing strongly with depth. A similar trend is observed in all models, with the exception of Schmandt et al. (2015) and Moschetti et al. (2010b) which show low v_S anomalies in the upper crust. This anomaly could be related to a mafic composition following continental rifting during the initiation of the Cascadia subduction zone (Catchings & Mooney, 1988a; Schmandt & Humphreys, 2011). It is worth noting that, as explained previously, we do not invert for sediment layers as they are too thin to be constrained by our data, which have a minimum period of 38 s. Therefore care must be taken when comparing our model with others at shallow depths (e.g., 5–10 km), the depths at which other models image sediments, while our images may show a mix of sediments and other deeper structures (Figures S15 and S16 in the Supporting Information S1). For example, the Columbia basin is covered by a thick layer of Miocene flood basalts (Catchings & Mooney, 1988a, 1988b) which we might have imaged in the upper crustal layer. This anomaly is similarly reflected in the upper sediments of Schmandt et al. (2015). We remind the reader however, that as previously explained, that the upper crustal layer will show a fix of sediments and crustal structure, especially where the sediment layer is thicker, such as in the Columbia basin.

In order to further explore the differences observed beneath the Columbia basin between our model and the model of Schmandt et al. (2015), we computed theoretical amplification curves for the input model of Schmandt et al. (2015) at the points of the model nearest to nine illustrative stations shown in Figure S17 in the Supporting Information S1. The same test was performed using the model made by Shen and Ritzwoller (2016), as shown in Figure S18 in the Supporting Information S1. These two models show the Columbia basin, in particular the Yakima Fold Belt in the western part of the basin, as largely a low-velocity anomaly in the upper crust. Therefore we ran a test to see if these models fit our observations. Forward modeling of these models shows that neither fits all data particularly well (Figures S17, S18 in the Supporting Information S1). The model of Shen and Ritzwoller (2016) fits the Love wave amplification curves well, but not the Rayleigh wave curves at short periods ($T \sim 35$–70 s). In contrast, the model of Schmandt et al. (2015) fits the Rayleigh wave data rather well, but not the

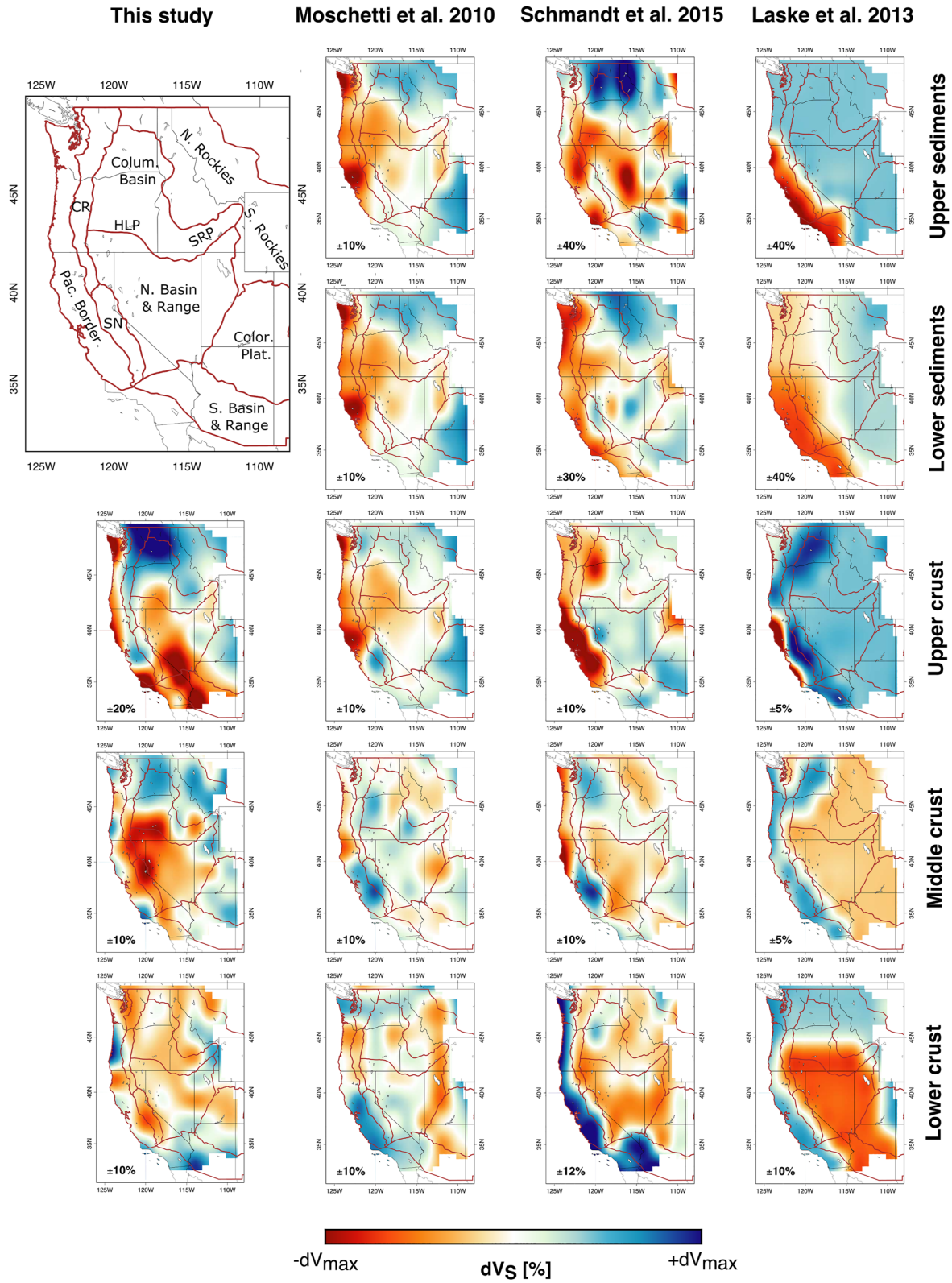

Figure 8. Comparison of the SWUS-crust v_S model (first column) with other layered crustal models, the model of Moschetti et al. (2010b), US-CrustVs-2015 (Schmandt et al., 2015) and CRUST1.0 (Laske et al., 2012). SWUS-crust does not constrain sedimentary layers, hence there are missing panels. In their place is a map showing the location of key tectonic features that are discussed. For each map, the velocity perturbations are presented with respect to the average velocity of that map. The limits of the perturbations are given in the bottom-left of each map and the boundaries of each tectonic province are shown by brown lines.

Love wave data. This test helps us to confirm that the surface wave amplification data require the observed fast v_S anomaly and that this anomaly is not due for example, to the model parameterization chosen. Both models use similar data types, so the observed differences could be due to their choice of inversion scheme.

The High Lava Plains (HLP in Figure 8), located in central Oregon, form a boundary between the Basin and Range province to the south and the Columbia basin to the north. This is also represented in Figure 8, where the HLP divide the high v_S anomalies of the Columbia basin with the low v_S anomalies of the North Basin and Range. In all layers of SWUS-crust, low v_S anomalies are observed beneath the HLP and the northern border is particularly well delineated in the middle crustal layer. The plains are also well delineated in CRUST1.0 but not in its upper crustal layer, while Moschetti et al. (2010b) only observed this low v_S anomaly in the upper crust. The anomaly observed in SWUS-crust throughout the entire crust may be explained by a magma injection due to recent volcanism along the Yellowstone hotspot track (Jordan et al., 2004).

The North Basin and Range appears largely as a low v_S anomaly throughout SWUS-crust (Figures 7 and 8). Most models show a similar feature, although at 10 km depth in Figure ??, large portions of the North Basin and Range show high v_S anomalies, in agreement with the model of Schmandt et al. (2015). Low v_S anomalies are consistent across all models in Figure 8 in the middle crust and between 20 and 30 km depth in Figure ?? This is with the exception of the thinnest parts of the North Basin and Range (see Figure S7 in the Supporting Information S1) at the northern border. Low v_S anomalies in the middle crust may be related to extensional deformation, as Moschetti et al. (2010a) imaged strong crustal anisotropy in this region. In the lower crust, low v_S anomalies may reflect Quaternary volcanism (Walker et al., 2004) and more recent intrusion of melts into the lower crust (Lin et al., 2014), which may produce an area of high heat flow (Tesauro et al., 2014).

Finally, the Colorado Plateau shows a largely high v_S anomaly in the upper and middle crust, generally agreeing with most other models in Figure 8, with the notable exception being the middle crust in CRUST1.0 (Laske et al., 2012). The fast v_S anomalies observed in this region may be attributed to the mafic composition of the plateau as discussed, for example, by Zandt et al. (1995). In addition, higher v_S anomalies in the center of the plateau compared to the boundaries in the upper crust may be related to cold temperatures, which is consistent with low heat flow measurements in the region (Blackwell & Richards, 2004). Figures S15 and S16 in the Supporting Information S1 show that at lower crustal depths (>25 km) the plateau is largely associated with a low v_S anomaly, matching almost all other models. As discussed by Moschetti et al. (2010b), it remains unclear if this is due to thermal or compositional effects.

4.3. Limitations and Future Work

While this work showed that crustal structure can be constrained by surface wave amplification data alone, the use of shorter period data is needed to image smaller-scale structures. For example, in order to invert for thin sedimentary layers, we could include ambient noise and ellipticity measurements to add sensitivity to the top few kilometers of the crust. Moreover, future joint inversions of amplification data along with surface wave dispersion measurements, ellipticity measurements and receiver functions would help to further constrain v_S in the crust, and also the depths of the crustal layers. This may also help to improve the data fit, particularly for seismic stations in the North Basin and Range, as the layer depths will no longer have to be fixed to CRUST1.0. Finally, while thanks to a careful data selection we could fit both Rayleigh and Love wave amplification data well, by incorporating further data types (dispersion, etc), in the future we may be able to constrain anisotropy in the mantle and crust. In turn, this could help significantly to interpret the model in terms of the tectonic and geodynamical evolution of the region.

5. Conclusions

We presented SWUS-crust, a crustal model of the western U.S. built with Rayleigh (T ~ 38–115 s) and Love (T ~ 38–63 s) wave amplification measurements. This is, to the best of our knowledge, the first time Love wave amplification measurements have been used to construct a seismic model. Thorough data selection and measurement techniques mean the data are not bias by source or path effects, including overtone interference. Love wave amplification measurements show a strong sensitivity to the crust and, when jointly inverted with Rayleigh wave amplification data using the Neighborhood Algorithm, lead to a crustal model that is more detailed than its predecessor model, SWUS-amp (Schardong et al., 2019).

Due to its complex tectonic history, significant variability in shear-wave velocity is imaged across the western U.S.. SWUS-crust clearly shows the fast Columbia basin in the upper and middle crust. Moreover, it shows distinct changes in velocity beneath the Colorado Plateau from generally high anomalies in the upper and mid crust, to lower anomalies in the lower crust, particularly at 30 km depth. We largely image the slow North Basin and Range throughout the whole crust. The High Lava Plains of central and south-eastern Oregon are imaged in finer detail compared to previous models. In particular, the northern border of the HLP in southern Oregon appears very well delineated in the middle layer of SWUS-crust.

Given that we observe many well-known seismic features the region, despite the relatively long-period data used compared to many of these studies, we suggest the inclusion of this data set can provide even higher-resolution images on crustal structure in the future.

Data Availability Statement

The surface wave amplification data set used in this study is attributed to Schardong et al. (2022). The Neighbourhood Algorithm (Sambridge, 1999) can be downloaded from http://iearth.edu.au/codes/NA/. The normal mode package used in this study is Mineos 1.0.2 (Masters et al., 2011) published under the GPL2 license and can be downloaded at http://geoweb.cse.ucdavis.edu/cig/software/mineos/. The authors thank the Computational Infrastructure for Geodynamics (http://geodynamics.org) which is funded by the National Science Foundation under awards EAR-0949446 and EAR-1550901. The other tomography models used in this study were obtained from the IRIS Earth Model Collaboration (http://ds.iris.edu/ds/products/emc-earthmodels/). ETOPO1 (Amante & Eakins, 2009) was downloaded from https://www.ngdc.noaa.gov/mgg/global/. All maps were built using Generic Mapping Tools (GMT) version 6 (Wessel et al., 2019) licensed under the LGPL version 3 or later, available at https://www.genericmapping-tools.org/. The seismic networks, that recorded the seismic data can be found here: TA (IRIS Transportable Array, 2003), US (Albuquerque Seismological Laboratory (ASL)/USGS, 1990), BK (Northern California Earthquake Data Center, 2014), CI (California Institute of Technology and United States Geological Survey Pasadena, 1926), AZ (Frank Vernon, 1982), NN (University of Nevada, Reno, 1971), IU (Albuquerque Seismological Laboratory/USGS, 2014), LI (California Institute of Technology (Caltech), 2000).

Acknowledgments
The authors thank Matthew Fox for fruitful discussion and for his insight into the kriging analysis. The authors also thank Eric Debayle and David Dobson for fruitful discussion. WS was supported by NERC grant number NE/L002485/1. AMGF is grateful to funding from the European Research Council (ERC) under the European Union's Horizon 2023 research and innovation program (grant agreement number 101001601). AM is supported by the STFC UCL Centre for Doctoral Training in Data Intensive Science (grant number ST/P006736/1). The authors gratefully acknowledge the availability of global seismograms from the IRIS Data Services and the IU, II, GEOFON, and GEOSCOPE networks. The seismic data analyses and inversions were carried out on the High Performance Computing Clusters Grace and Kathleen, supported by the Research and Computing Support services at UCL. The authors thank Hendrik van Heijst for providing his surface wave amplitude measurements.

References

Albuquerque Seismological Laboratory (ASL)/USGS (1990). United States national seismic network. International Federation of Digital Seismograph Networks. https://doi.org/10.7914/SN/US

Albuquerque Seismological Laboratory/USGS (2014). Global seismograph network (gsn−iris/usgs). International Federation of Digital Seismograph Networks. https://doi.org/10.7914/SN/IU

Amante, C., & Eakins, B. W. (2009). Etopo1 arc-minute global relief model: Procedures, data sources and analysis. https://doi.org/10.7289/V5C8276M

Ariyanto, P., Rosid, S., Anggono, T., Januarti, Y., & Januarti, Y. (2018). Crustal structure in the southern part of central java based on analysis of tele-seismic receiver function using a neighbourhood algorithm. *Journal of Physics: Conference Series*, *985*, 012018. https://doi.org/10.1088/1742-6596/985/1/012018

Attanayake, J., Ferreira, A. M., Berbellini, A., & Morelli, A. (2017). Crustal structure beneath portugal from teleseismic rayleigh wave ellipticity. *Tectonophysics*, *712*, 344–361. https://doi.org/10.1016/j.tecto.2017.06.001

Bao, X., Dalton, C. A., & Ritsema, J. (2016). Effects of elastic focusing on global models of rayleigh wave attenuation. *Geophysical Supplements to the Monthly Notices of the Royal Astronomical Society*, *207*(2), 1062–1079. https://doi.org/10.1093/gji/ggw322

Bassin, C. (2000). The current limits of resolution for surface wave tomography in North America. *Eos, Transactions, American Geophysical Union, 81: Fall Meet Supply, Abstract*.

Bateman, P. C., & Eaton, J. P. (1967). Sierra nevada batholith: The batholith was generated within a synclinorium. *Science*, *158*(3807), 1407–1417. https://doi.org/10.1126/science.158.3807.1407

Bensen, G., Ritzwoller, M., & Yang, Y. (2009). A 3-d shear velocity model of the crust and uppermost mantle beneath the United States from ambient seismic noise. *Geophysical Journal International*, *177*(3), 1177–1196. https://doi.org/10.1111/j.1365-246x.2009.04125.x

Berbellini, A., Morelli, A., & Ferreira, A. M. (2017). Crustal structure of northern Italy from the ellipticity of rayleigh waves. *Physics of the Earth and Planetary Interiors*, *265*, 1–14. https://doi.org/10.1016/j.pepi.2016.12.005

Blackwell, D., & Richards, M. (2004). Geothermal map of North America. In *American association of petroleum geologist (aapg), 1 sheet, scale 1: 6,500,000. Search In*.

Braile, L., Hinze, W., Von Frese, R., & Keller, G. R. (1989). Seismic properties of the crust and uppermost mantle of the conterminous United States and adjacent Canada. *Geological Society of America Memoir*, *172*, 655–680. https://doi.org/10.1130/mem172-p655

Brocher, T. M. (2005). Empirical relations between elastic wavespeeds and density in the earth's crust. *Bulletin of the Seismological Society of America*, *95*(6), 2081–2092. https://doi.org/10.1785/0120050077

Buehler, J., & Shearer, P. (2012). Localized imaging of the uppermost mantle with usarray pn data. *Journal of Geophysical Research*, *117*(B9), B09305. https://doi.org/10.1029/2012jb009433

California Institute of Technology and United States Geological Survey Pasadena (1926). Southern California seismic network. International Federation of Digital Seismograph Networks. https://doi.org/10.7914/SN/CI

California Institute of Technology (Caltech) (2000). Laser interferometer gravitational-wave experiment. International Federation of Digital Seismograph Networks. https://doi.org/10.7914/SN/LI

Catchings, R., & Mooney, W. (1988). Crustal structure of the columbia plateau: Evidence for continental rifting. *Journal of Geophysical Research*, *93*(B1), 459–474. https://doi.org/10.1029/jb093ib01p00459

Catchings, R., & Mooney, W. D. (1988). Crustal structure of east central Oregon: Relation between newberry volcano and regional crustal structure. *Journal of Geophysical Research*, *93*(B9), 10081–10094. https://doi.org/10.1029/jb093ib09p10081

Chai, C., Ammon, C. J., Maceira, M., & Herrmann, R. B. (2015). Inverting interpolated receiver functions with surface wave dispersion and gravity: Application to the western us and adjacent Canada and Mexico. *Geophysical Research Letters*, *42*(11), 4359–4366. https://doi.org/10.1002/2015gl063733

Chang, S.-J., Ferreira, A. M., Ritsema, J., Van Heijst, H. J., & Woodhouse, J. H. (2015). Joint inversion for global isotropic and radially anisotropic mantle structure including crustal thickness perturbations. *Journal of Geophysical Research: Solid Earth*, *120*(6), 4278–4300. https://doi.org/10.1002/2014jb011824

Christensen, N. I., & Mooney, W. D. (1995). Seismic velocity structure and composition of the continental crust: A global view. *Journal of Geophysical Research*, *100*(B6), 9761–9788. https://doi.org/10.1029/95jb00259

Christiansen, R. L., Foulger, G., & Evans, J. R. (2002). Upper-mantle origin of the yellowstone hotspot. *Geological Society of America Bulletin*, *114*(10), 1245–1256. https://doi.org/10.1130/0016-7606(2002)114<1245:umooty>2.0.co;2

Dalton, C. A., Bao, X., & Ma, Z. (2017). The thermal structure of cratonic lithosphere from global rayleigh wave attenuation. *Earth and Planetary Science Letters*, *457*, 250–262. https://doi.org/10.1016/j.epsl.2016.10.014

Dziewonski, A. M., & Anderson, D. L. (1981). Preliminary reference earth model. *Physics of the Earth and Planetary Interiors*, *25*(4), 297–356. https://doi.org/10.1016/0031-9201(81)90046-7

Eddy, C. L., & Ekström, G. (2014). Local amplification of rayleigh waves in the continental United States observed on the usarray. *Earth and Planetary Science Letters*, *402*, 50–57. https://doi.org/10.1016/j.epsl.2014.01.013

Ferreira, A. M., Marignier, A., Attanayake, J., Frietsch, M., & Berbellini, A. (2020). Crustal structure of the azores archipelago from rayleigh wave ellipticity data. *Geophysical Journal International*, *221*(2), 1232–1247. https://doi.org/10.1093/gji/ggaa076

Ferreira, A. M., & Woodhouse, J. H. (2007). Observations of long period rayleigh wave ellipticity. *Geophysical Journal International*, *169*(1), 161–169. https://doi.org/10.1111/j.1365-246x.2006.03276.x

Ferreira, A. M., Woodhouse, J. H., Visser, K., & Trampert, J. (2010). On the robustness of global radially anisotropic surface wave tomography. *Journal of Geophysical Research*, *115*(B4), B04313. https://doi.org/10.1029/2009jb006716

Frank, V. (1982). Anza regional network. International Federation of Digital Seismograph Networks. https://doi.org/10.7914/SN/AZ

Frietsch, M., Ferreira, A. M., & Funning, G. J. (2021). Data-driven two-fault modeling of the mw 6.0 2008 wells, nevada earthquake suggests a listric fault rupture. *Journal of Geophysical Research: Solid Earth*, *126*(4), e2020JB020263. https://doi.org/10.1029/2020jb020263

Gilbert, F. (1971). Excitation of the normal modes of the earth by earthquake sources. *Geophysical Journal International*, *22*(2), 223–226. https://doi.org/10.1111/j.1365-246x.1971.tb03593.x

Gilbert, H. (2012). Crustal structure and signatures of recent tectonism as influenced by ancient terranes in the western United States. *Geosphere*, *8*(1), 141–157. https://doi.org/10.1130/ges00720.1

Hariharan, A., Dalton, C. A., Babikoff, J., & Ekström, G. (2022). Controls on surface wave overtone interference. *Geophysical Journal International*, *228*(3), 1665–1683.

Hariharan, A., Dalton, C. A., Ma, Z., & Ekström, G. (2020). Evidence of overtone interference in fundamental-mode rayleigh wave phase and amplitude measurements. *Journal of Geophysical Research: Solid Earth*, *125*(1), e2019JB018540. https://doi.org/10.1029/2019jb018540

Hildreth, W. (2007). *Quaternary magmatism in the cascades: Geologic perspectives*. US Geological Survey.

Huber, N. K. (1981). Amount and timing of late cenozoic uplift and tilt of the central sierra Nevada, California; evidence from the upper san joaquin river basin.

Humphreys, E. D., & Coblentz, D. D. (2007). North american dynamics and western us tectonics. *Reviews of Geophysics*, *45*(3), RG3001. https://doi.org/10.1029/2005rg000181

IRIS Transportable Array (2003). Usarray transportable array. International Federation of Digital Seismograph Networks. https://doi.org/10.7914/SN/TA

Jones, G. A., Ferreira, A. M., Kulessa, B., Schimmel, M., Berbellini, A., & Morelli, A. (2021). Uppermost crustal structure regulates the flow of the Greenland ice sheet. *Nature Communications*, *12*(1), 1–12. https://doi.org/10.1038/s41467-021-27537-5

Jordan, B. T., Grunder, A. L., Duncan, R. A., & Deino, A. L. (2004). Geochronology of age-progressive volcanism of the Oregon high lava plains: Implications for the plume interpretation of yellowstone. *Journal of Geophysical Research*, *109*(B10), B10202. https://doi.org/10.1029/2003jb002776

Laske, G., Masters, G., Ma, Z., & Pasyanos, M. (2012). Crust1. 0: An updated global model of earth's crust. *Geophysical Research Abstracts*, *14*, 3743.

Laske, G., Masters, G., Ma, Z., & Pasyanos, M. (2013). Update on crust1. 0—A 1-degree global model of earth's crust. *Geophysical Research Abstracts*, *15*, 2658.

Lin, F.-C., Moschetti, M. P., & Ritzwoller, M. H. (2008). Surface wave tomography of the western United States from ambient seismic noise: Rayleigh and love wave phase velocity maps. *Geophysical Journal International*, *173*(1), 281–298. https://doi.org/10.1111/j.1365-246x.2008.03720.x

Lin, F.-C., Tsai, V. C., & Ritzwoller, M. H. (2012). The local amplification of surface waves: A new observable to constrain elastic velocities, density, and anelastic attenuation. *Journal of Geophysical Research*, *117*(B6), B06302. https://doi.org/10.1029/2012jb009208

Lin, F.-C., Tsai, V. C., & Schmandt, B. (2014). 3-d crustal structure of the western United States: Application of rayleigh-wave ellipticity extracted from noise cross-correlations. *Geophysical Journal International*, *198*(2), 656–670. https://doi.org/10.1093/gji/ggu160

Masters, G., Woodhouse, J., & Freeman, G. (2011). Mineos v1. 0.2 [software]. *Computational Infrastructure for Geodynamics*. Retrieved from https://geodynamics.org/cig/software/mineos/

Moschetti, M., Ritzwoller, M., Lin, F., & Yang, Y. (2010). Seismic evidence for widespread western-us deep-crustal deformation caused by extension. *Nature*, *464*(7290), 885–889. https://doi.org/10.1038/nature08951

Moschetti, M., Ritzwoller, M., Lin, F.-C., & Yang, Y. (2010). Crustal shear wave velocity structure of the western United States inferred from ambient seismic noise and earthquake data. *Journal of Geophysical Research*, *115*(B10), B10306. https://doi.org/10.1029/2010jb007448

Moschetti, M., Ritzwoller, M., & Shapiro, N. (2007). Surface wave tomography of the western United States from ambient seismic noise: Rayleigh wave group velocity maps. *Geochemistry, Geophysics, Geosystems*, *8*(8), Q08010. https://doi.org/10.1029/2007gc001655

Northern California Earthquake Data Center (2014). Berkeley digital seismic network (bdsn). Northern California Earthquake Data Center. https://doi.org/10.7932/BDSN

Pasyanos, M. E., Masters, T. G., Laske, G., & Ma, Z. (2014). Litho1. 0: An updated crust and lithospheric model of the earth. *Journal of Geophysical Research: Solid Earth*, *119*(3), 2153–2173. https://doi.org/10.1002/2013jb010626

Porter, R., Liu, Y., & Holt, W. E. (2016). Lithospheric records of orogeny within the continental US. *Geophysical Research Letters*, *43*(1), 144–153. https://doi.org/10.1002/2015gl066950

Rudnick, R., & Gao, S. (2014). Composition of the continental crust. In *Treatise on geochemistry* (Vol. 4, pp. 1–51). Elsevier. https://doi.org/10.1016/b978-0-08-095975-7.00301-6

Sambridge, M. (1999). Geophysical inversion with a neighbourhood algorithm—I. Searching a parameter space. *Geophysical Journal International*, *138*(2), 479–494. https://doi.org/10.1046/j.1365-246x.1999.00876.x

Schaeffer, A., & Lebedev, S. (2015). Global heterogeneity of the lithosphere and underlying mantle: A seismological appraisal based on multimode surface-wave dispersion analysis, shear-velocity tomography, and tectonic regionalization. In *The earth's heterogeneous mantle* (pp. 3–46). Springer. https://doi.org/10.1007/978-3-319-15627-9_1

Schardong, L., Ferreira, A. M., Berbellini, A., & Sturgeon, W. (2019). The anatomy of uppermost mantle shear-wave speed anomalies in the western us from surface-wave amplification. Earth and Planetary Science Letters, *528*, 115822. https://doi.org/10.1016/j.epsl.2019.115822

Schardong, L., Sturgeon, W., Ferreira, A. M., & Berbellini, A. (2022). WUSA surface wave amplification measurements (Schardong et al. 2019). Zenodo. https://doi.org/10.5281/zenodo.7352566

Schellart, W., Stegman, D., Farrington, R., Freeman, J., & Moresi, L. (2010). Cenozoic tectonics of western North America controlled by evolving width of farallon slab. *Science*, *329*(5989), 316–319. https://doi.org/10.1126/science.1190366

Schmandt, B., & Humphreys, E. (2011). Seismically imaged relict slab from the 55 ma siletzia accretion to the northwest United States. *Geology*, *39*(2), 175–178. https://doi.org/10.1130/g31558.1

Schmandt, B., Lin, F.-C., & Karlstrom, K. E. (2015). Distinct crustal isostasy trends east and west of the rocky mountain front. *Geophysical Research Letters*, *42*(23), 10–290. https://doi.org/10.1002/2015gl066593

Shapiro, N. M., Campillo, M., Stehly, L., & Ritzwoller, M. H. (2005). High-resolution surface-wave tomography from ambient seismic noise. *Science*, *307*(5715), 1615–1618. https://doi.org/10.1126/science.1108339

Shen, W., & Ritzwoller, M. H. (2016). Crustal and uppermost mantle structure beneath the United States. *Journal of Geophysical Research: Solid Earth*, *121*(6), 4306–4342. https://doi.org/10.1002/2016jb012887

Shen, W., Ritzwoller, M. H., & Schulte-Pelkum, V. (2013). A 3-d model of the crust and uppermost mantle beneath the central and western us by joint inversion of receiver functions and surface wave dispersion. *Journal of Geophysical Research: Solid Earth*, *118*(1), 262–276. https://doi.org/10.1029/2012jb009602

Stewart, J. H. (1980). *Geology of nevada* (Vol. 4, pp. 136). Nevada Bureau of Mines and Geology Special publication.

Szwillus, W., Afonso, J. C., Ebbing, J., & Mooney, W. D. (2019). Global crustal thickness and velocity structure from geostatistical analysis of seismic data. *Journal of Geophysical Research: Solid Earth*, *124*(2), 1626–1652. https://doi.org/10.1029/2018jb016593

Taylor, S. R., Gerstoft, P., & Fehler, M. C. (2009). Estimating site amplification factors from ambient noise. *Geophysical Research Letters*, *36*(9). https://doi.org/10.1029/2009gl037838

Tesauro, M., Kaban, M. K., Mooney, W. D., & Cloetingh, S. (2014). Nacr14: A 3d model for the crustal structure of the North American continent. *Tectonophysics*, *631*, 65–86. https://doi.org/10.1016/j.tecto.2014.04.016

University of Nevada, Reno (1971). Nevada seismic network. International federation of digital seismograph networks. https://doi.org/10.7914/SN/NN

Van Heijst, H. J., & Woodhouse, J. (1997). Measuring surface-wave overtone phase velocities using a mode-branch stripping technique. *Geophysical Journal International*, *131*(2), 209–230. https://doi.org/10.1111/j.1365-246x.1997.tb01217.x

Voronoï, G. (1908). Nouvelles applications des parametres continus a la theorie des forms quadratiques. deuxieme memoire: Recheches sur les parallelloedres primitifs. *Journal für die Reine und Angewandte Mathematik*, *134*, 198–287. https://doi.org/10.1515/crll.1908.134.198

Walker, J. D., Bowers, T. D., Glazner, A. F., Farmer, A., & Carlson, R. W. (2004). Creation of a North American volcanic and plutonic rock database (navdat). *Geological Society of America Abstracts with Programs*, *36*(9).

Wessel, P., Luis, J., Uieda, L., Scharroo, R., Wobbe, F., Smith, W. H., & Tian, D. (2019). The generic mapping tools version 6. Geochemistry, Geophysics, Geosystems, *20*, 5556–5564. https://doi.org/10.1029/2019gc008515

Xie, J., Chu, R., & Yang, Y. (2018). 3-d upper-mantle shear velocity model beneath the contiguous United States based on broadband surface wave from ambient seismic noise. *Pure and Applied Geophysics*, *175*(10), 3403–3418. https://doi.org/10.1007/s00024-018-1881-2

Yudistira, T., Paulssen, H., & Trampert, J. (2017). The crustal structure beneath The Netherlands derived from ambient seismic noise. *Tectonophysics*, *721*, 361–371. https://doi.org/10.1016/j.tecto.2017.09.025

Zandt, G., Myers, S. C., & Wallace, T. C. (1995). Crust and mantle structure across the basin and range-Colorado plateau boundary at 37N latitude and implications for cenozoic extensional mechanism. *Journal of Geophysical Research*, *100*(B6), 10529–10548. https://doi.org/10.1029/94jb03063